Available online at www.sciencedirect.com

SCIENCE DIRECT®

Remote Sensing of Environment 92 (2004) 521–534

Remote Sensing of Environment

www.elsevier.com/locate/rse

Deriving land surface temperature from Landsat 5 and 7 during SMEX02/SMACEX

Fuqin Li[a,*] Thomas J. Jackson[a] William P. Kustas[a] Thomas J. Schmugge[a]
Andrew N. French[b] Michael H. Cosh[a] Rajat Bindlish[a]

[a] *USDA-ARS Hydrology and Remote Sensing Laboratory, Room 104, Building 007 BARC-West, Beltsville, MD 20705, USA*
[b] *Hydrological Sciences Branch, NASA Goddard Space Flight Center, USA*

Received 22 July 2003; received in revised form 19 November 2003; accepted 18 February 2004

Abstract

A sequence of five high-resolution satellite-based land surface temperature (T_s) images over a watershed area in Iowa were analyzed. As a part of the SMEX02 field experiment, these land surface temperature images were extracted from Landsat 5 Thematic Mapper (TM) and Landsat 7 Enhanced Thematic Mapper (ETM) thermal bands. The radiative transfer model MODTRAN 4.1 was used with atmospheric profile data to atmospherically correct the Landsat data. NDVI derived from Landsat visible and near-infrared bands was used to estimate fractional vegetation cover, which in turn was used to estimate emissivity for Landsat thermal bands. The estimated brightness temperature was compared with concurrent tower based measurements. The mean absolute difference (MAD) between the satellite-based brightness temperature estimates and the tower based brightness temperature was 0.98 °C for Landsat 7 and 1.47 °C for Landsat 5, respectively. Based on these images, the land surface temperature spatial variation and its change with scale are addressed. The scaling properties of the surface temperature are important as they have significant implications for changes in land surface flux estimation between higher-resolution Landsat and regional to global sensors such as MODIS.
Published by Elsevier Inc.

Keywords: Land surface temperature; Landsat 5 Thematic Mapper; Landsat 7 Enhanced Thematic Mapper

1. Introduction

Land surface temperature (T_s) is a key boundary condition in many remote sensing-based land surface modeling schemes (Kustas & Norman, 1996). Currently available satellite thermal infrared sensors provide different spatial resolution and temporal coverage data that can be used to estimate land surface temperature. The Geostationary Operational Environmental Satellite (GOES) has a 4-km resolution in the thermal infrared, while the NOAA-Advanced Very High Resolution Radiometer (AVHRR) and the Terra and Aqua-Moderate Resolution Imaging Spectroradiometer (MODIS) have 1-km spatial resolutions. Significantly high-resolution data come from the Terra-Advanced Spaceborne Thermal Emission and Reflection Radiometer (ASTER) which has a 90-m pixel resolution, the Landsat-5 Thematic Mapper (TM) which has a 120-m resolution, and Landsat-7 Enhanced Thematic Mapper (ETM) which has a 60-m resolution. However, these instruments have a repeat cycle of 16 days.

It is possible that these different sources of data can be used synergistically. Higher-resolution and less frequent thermal infrared observations from Landsat might be used to understand the spatial variation within coarser-resolution observations made by MODIS and AVHRR, which provide more frequent measurements. This spatial information is important in estimating energy balance components, which utilize temperature measurements, because it is known that (unlike the measured radiance) the fluxes do not exhibit linear scaling (Bresnahan & Miller, 1997). The flux computed from an average coarse resolution observation is not the same as the total of the fluxes computed from higher-resolution observations (Bresnahan & Miller, 1997). The errors introduced, however, depend on meteorological conditions and the scale and magnitude of the surface contrast at the subpixel or subgrid resolution (Kustas & Norman, 2000).

* Corresponding author. Tel.: +1-301-504-7614; fax: +1-301-504-8931.
E-mail address: fcl@hydrolab.arsusda.gov (F. Li).

0034-4257/$ - see front matter. Published by Elsevier Inc.
doi:10.1016/j.rse.2004.02.018

In this paper, we analyzed several aspects of integrating these various satellite data sources using data collected as part of the Soil Moisture Experiments in 2002 (SMEX02, http://hydrolab.arsusda.gov/smex02). SMEX02 was conducted during the summer over central Iowa croplands. These analyses will require reliable estimates of T_s, which in turn requires atmospheric correction of the satellite data and estimation of surface emissivity (Gillespie et al., 1998; Schmugge et al., 1998; Wan et al., 2002). Newer satellite systems, e.g., MODIS and ASTER include features to allow easier calibration and provide T_s as standard products. This is not true for the Landsat data. Therefore, as a first step in this analysis for the SMEX02 data sets, available high-resolution satellite sources of T_s observations were calibrated. These include Landsat TM and ETM data. Validation was provided using ground based surface temperature, low altitude aircraft temperature data and ASTER estimates of surface emissivity (ε_λ). These computations required atmospheric correction to convert radiance to brightness temperature and estimates of emissivity to convert brightness temperature to T_s.

The MODTRAN 4.1 radiative transfer model (Berk et al., 1998) is used with atmospheric profile data to atmospherically correct the Landsat data and ancillary information, as described later, for extracting ε_λ. The derived high-resolution remotely sensed surface brightness temperatures are compared to ground-based remote sensing observations of surface brightness temperature. Changes in T_s and fractional vegetation cover due to the rapid growth in the corn and soybean crops are described, analyzed and discussed.

In addition, spatial variations of T_s at different pixel resolutions are analyzed and discussed. Changes in variability of T_s with scale is evaluated since this variability has an impact on estimates of land surface fluxes derived from remote sensing based surface energy balance models (Kustas & Norman, 1996). The analysis of scaling of T_s can be used to study how more spatially detailed results from TM/ETM can be compared with the lower-resolution data such as Terra-MODIS data (which are acquired a short time after Landsat). In future work, these results will be combined with other data and used to investigate how fluxes are affected by the scale or resolution of T_s from operational satellites, such as MODIS and GOES.

2. Study area description and data sets

2.1. SMEX02

SMEX02 was a soil moisture and water cycle field campaign conducted in central Iowa between mid-June and mid-July, 2002. SMEX02 covered a range of spatial scales from within field sampling of surface soil moisture, vegetation biomass and cover, flux measurements at the field scale using tower measurements, and at the watershed and regional scale with aircraft-based measurements. Optical and microwave remote sensing data were acquired at pixel resolutions ranging from 1 m to a few kilometers with aircraft-based sensors and at tens of meters to tens of kilometers from satellite-based sensors. Details of the experiment can be found at website (http://hydrolab.arsusda.gov/smex02).

SMEX02 data used for this paper include the Landsat 5 TM, Landsat 7 ETM, ASTER thermal bands, MODIS land surface temperature data, and radiosonde data within the study area and from the nearest operational sounding. In addition, radiometric surface temperature data from tower-based and aircraft-based sensors on the Canadian Twin Otter were used.

2.2. Regional and watershed areas

In order to satisfy a variety of research objectives, two study areas were selected. One was a region called the Iowa study area and the other was a watershed, called the Walnut Creek (WC) watershed study area. The WC study area was 18 km North–South × 36 km East–West south of Ames, IA. The upper left coordinate is 93.832437 W and 42.729216 N and the low right coordinate is 93.391061 W and 41.875254 N.

The WC area was the primary focus of the Soil Moisture Atmosphere Coupling Experiment (SMACEX) and analyses conducted here. Fourteen flux towers were located within the area and the Canadian Twin Otter (MacPherson & Wolde, 2002) flew several flight tracks over the study site for evaluating spatial variability in fluxes across the watershed (see Fig. 1).

In 2002, nearly 95% of the WC was covered by row crops. Corn and soybean were the main crop varieties, with 50% in corn, ~ 40% in soybean, and the remaining ~ 10% in forage and grains. The climate is humid and the average annual rainfall is around 835 mm with one third of the rainfall typically occurring during May and June.

2.3. Radiometric surface temperature data from the flux towers

Broadband thermal infrared thermometer (IRT) observations were made with an Apogee instrument (model IRTS-P). [Note: Company and trade names were given for the benefit of the reader and imply no endorsement by USDA.] This broadband thermal infrared thermometer has a full wavelength range from 6.5 to 14 μm (but filtered to 8–14 μm) and was installed at 12 of the 14 flux tower locations within the WC study area. The accuracy of the instrument is reported to be ± 0.4 °C from 5 to 45 °C and ± 0.1 °C when the sensor body and target are at the same temperature. Detailed information about this instrument is provided on the web (http://www.apogee-inst.com/) and in Bugbee et al. (1999).

The IRTs were mounted at nominal heights of 2 m above ground level (agl) over soybean and 5 m agl over corn with a nadir view. With a field of view of approximately 1 to 1, and a soybean crop height of 0.5 m, this resulted in a

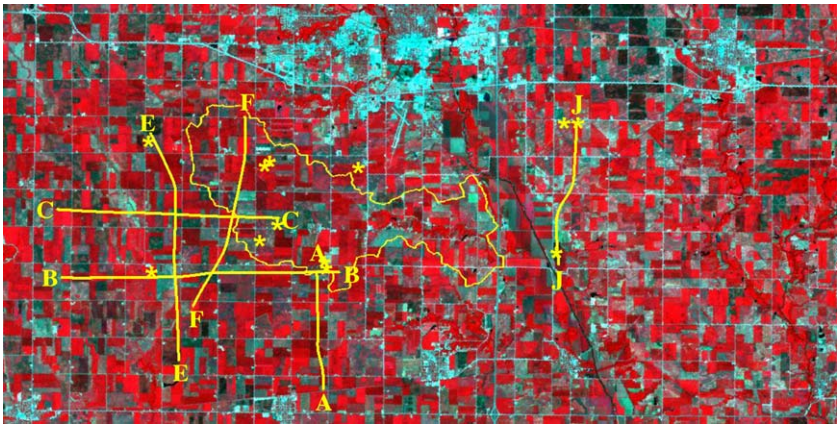

Fig. 1. Fourteen flux tower locations and Twin Otter tracks on the July 1, 2002 Landsat images over watershed area (thin yellow line is the Walnut Creek watershed, yellow stars are the location of flux towers and thick yellow lines are aircraft tracks).(For interpretation of the references to colour in this figure legend, the reader is referred to the web version of this article.)

sampling area or pixel size of roughly 1.5 m in diameter. For corn which grew rapidly from ~0.5 m at the start of the SMACEX field campaign to ~2 m by July 16, the diameter of the sampling area changed from 4.5 to 3 m.

2.4. Radiosonde data

As part of the field experiment, radiosonde atmospheric profiles of pressure, temperature, and water vapor were collected in the central part of the WC area (42.00 N, 93.61 W). Data were collected between June 15 and July 9, 2002. The radiosonde data used for atmospheric correction were collected within 2 h of Landsat/ASTER overpasses during these days. On the other days with Landsat coverage, July 16 and 17, radiosonde data from the two nearest operational sounding stations were acquired. The stations are Omaha/Valley, NE (station number 94980, 41.32N, 96.23W) and Davenport Municipal AP, IA (station number 94982, 41.60N, 90.57W). Radiosonde data from the two stations were interpolated to the same heights and then data from the two stations were averaged to provide input to the atmospheric correction models. Since the operational sounding data were only available at 0 and 12 GMT standard time, the closest time to the satellite overpasses, 12 GMT was used. The time difference between these radiosonde data and the satellite overpass were 4–5 h.

2.5. Aircraft-based IRT measurements from the Canadian Twin Otter

An IRT was installed on the Canadian Twin Otter for measuring surface temperature from an altitude of approximately 40 m agl. The waveband of the instrument is 9.6–11.5 μm. It has a 2.7° FOV with an accuracy of ~0.5 °C (see http://www.wintron.com/Infrared/kt19spec.htm). With a flying height of around 40 m agl and a nadir view, the diameter of the sampling area was about 4 m. Since the IRT observations were sampled at 32 Hz, the data were averaged along the flight track to yield 60 m segments for comparing with the satellite-derived land surface temperatures. MacPherson and Wolde (2002) provide further details about the flights and how the surface temperature was calculated.

2.6. Satellite data

During the SMEX02/SMACEX field campaign, two Landsat 5 TM and three Landsat 7 ETM scenes were acquired over the WC study area. The wavelengths of the thermal bands for both TM and ETM are 10.4–12.5 μm. These data were used to produce high-resolution (60 m for ETM and 120 m for TM) land surface temperature data products with the two thermal channels (high and low gain) of the ETM and the single thermal channel of the TM. At the same time, NDVI calculated from corrected surface reflectance from bands 3 and 4 were used to calculate the fractional vegetation cover (Choudhury et al., 1994). Details of the Landsat scenes are listed in Table 1. An ASTER image was also collected on July 1, 2002. ASTER has five thermal bands within a wavelength range from 8 to 12 μm. To compare the scaling results, one MODIS land surface temperature image was also obtained over the watershed area.

3. Approaches for estimating land surface temperature

There are three commonly used methods to retrieve T_s, depending mostly on how the sensor thermal bands were

Table 1
Landsat TM coverage for SMEX02

Date	Landsat no.	Path	Row
June 23, 2002	5	26	31
July 1, 2002	7	26	31
July 8, 2002	7	27	31
July 16, 2002	5	27	31
July 17, 2002	7	26	31

designed. These are the split window method, such as is used for NOAA–AVHRR data (Becker & Li, 1990), the day/night pairs of thermal infrared data in several bands, such as are used for MODIS (Wan et al., 2002) and single band correction (Price, 1983). Some satellites have multi-thermal bands, which allow simultaneous estimation of surface emissivity ε_λ and T_s.

A number of methods have been developed to separate ε_λ and T_s using multi-thermal band data (Li et al., 1999). Examples of sensors with multiple thermal bands include ASTER and MODIS. Methods used to analyze the data include the reference channel method (Kahle et al., 1980), the emissivity normalization method (Gillespie, 1985; Realmuto, 1990), the spectral ratio method (Watson, 1992), the alpha residuals method (Kealy & Gabell, 1990), and the temperature and emissivity separation algorithm (Gillespie et al., 1998; Schmugge et al., 2002). However, for satellites with a single thermal band, such as Landsat TM and ETM, obtaining T_s is more difficult. In addition to an accurate radiative transfer model and some knowledge of the atmospheric profile, ε_λ information is also required. For this reason, Landsat TM/ETM thermal data have not been widely used for temperature mapping although they have high spatial resolution (Qin et al., 2001). As a result, extensive processing and analysis of the Landsat data was required. The procedure and results are outlined in Fig. 2 and described in the following sections.

4. Atmospheric correction and calibration of Landsat thermal data

The TM/ETM images were level 1G products, partly geo-registered and also radiometrically corrected. However, the data were not corrected for atmospheric effects. The data are satellite-based digital numbers, which can be calibrated to sensor radiance using $I_\lambda = a + b \times \mathrm{DN}$, where I_λ is radiance at the sensor, a is offset, b is gain, and DN is the digital number from the image. If information about the atmospheric profile (especially water vapor) is known, this satellite-based radiance can be corrected to ground-based radiance using a radiative transfer model.

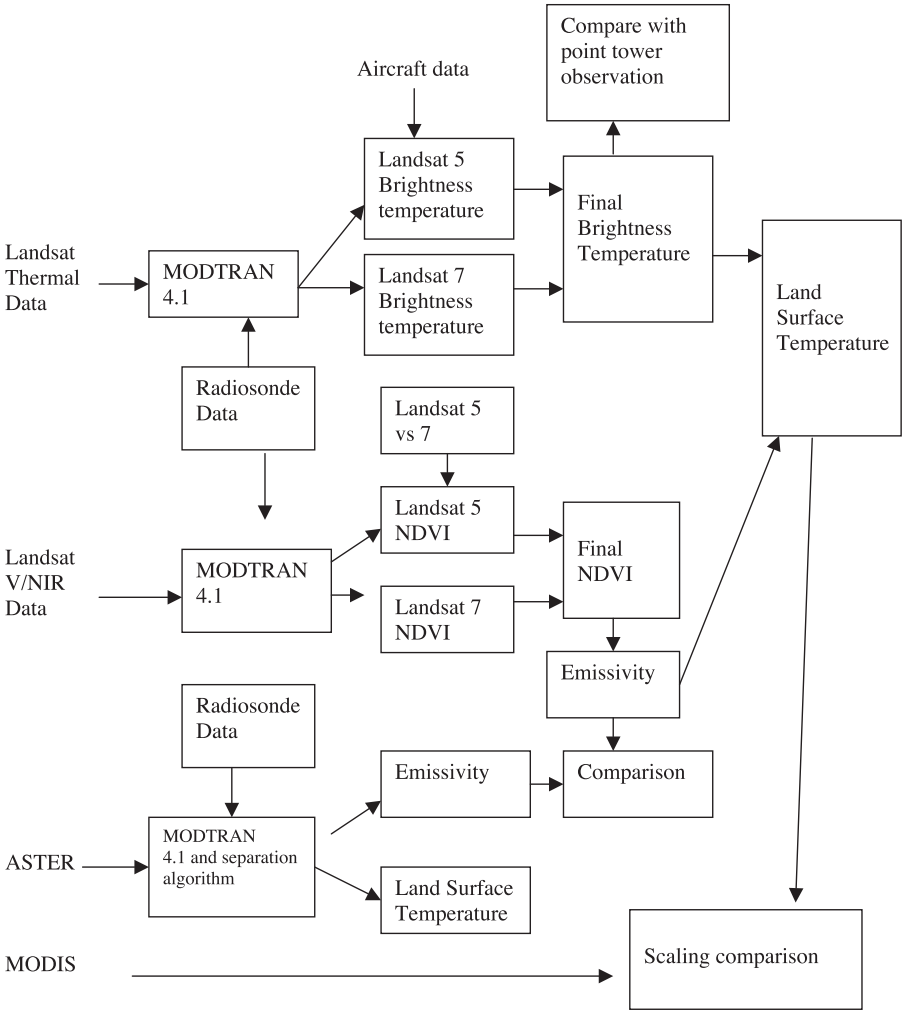

Fig. 2. Flowchart for estimation and verification of land surface temperature from satellite data.

Table 2
Atmospheric correction for Landsat 5 and 7 (thermal bands)

Date	Satellite	t_λ	d_λ (W m^{-2} sr^{-1} μm^{-1})	$I_{d\lambda}$ (W m^{-2} sr^{-1} μm^{-1})
June 23, 2002	Landsat 5	0.6925	2.5082	3.9513
July 1, 2002	Landsat 7	0.6127	3.1751	4.8249
July 8, 2002	Landsat 7	0.5371	3.6956	5.7257
July 16, 2002	Landsat 5	0.6594	2.7202	4.1743
July 17, 2002	Landsat 7	0.5636	3.5038	5.2668

4.1. Basic radiative transfer for thermal data

The sensor radiance I_λ can be expressed as (Schmugge et al., 1998):

$$I_\lambda = t_\lambda I_\lambda(0) + d_\lambda \quad (1)$$

where t_λ is atmospheric transmittance, d_λ is the spectral radiance added by the atmosphere, and $I_\lambda(0)$ is the surface leaving radiance.

The temperature corresponding to a black body radiator emitting the same radiance is called the brightness temperature (T_B). The radiance data can be converted into equivalent brightness temperatures. However, more generally the surface leaving radiance can be expressed in terms of surface temperature as:

$$I_\lambda(0) = I_\lambda^B(T_B) = \varepsilon_\lambda I_\lambda^B(T_s) + (1-\varepsilon_\lambda) I_{d\lambda} \quad (2)$$

where ε_λ is the surface emissivity (wavelength dependent), $I_{d\lambda}$ is the down-welling sky radiance due to the atmosphere, and $I_\lambda^B(T_s)$ is the spectral radiance from a blackbody at surface temperature T_s.

Using the atmospheric radiative transfer model MODTRAN (Berk et al., 1998), t_λ, d_λ, and $I_{d\lambda}$ can be obtained using the Landsat band response functions and the radiosonde data previously presented with the default aerosol values provided in the model. Table 2 lists t_λ, d_λ, and $I_{d\lambda}$.

Based on the Planck function, the relationship between the radiance at a single wavelength and blackbody temperature (brightness temperature) is

$$T_j = \frac{C_2}{\lambda_j \ln[C_1 / I_j \lambda_j^5 \pi + 1]} \quad (3)$$

where C_1 and C_2 are 3.74151×10^{-16} (W m^2) and 0.0143879 (m K), respectively, and I_j (W m^{-2}) is radiance at wavelength λ_j (m).

The relationship between band radiance and brightness temperature is complex. For a given waveband, let $W(\lambda)$ represent the response function and $\int_0^\infty W(\lambda')\mathrm{d}\lambda = 1$, then radiance at a waveband (I_w) can be expressed as:

$$I_w = \int_0^\infty W(\lambda') I_{\lambda'}[T]\mathrm{d}\lambda' \quad (4)$$

Among various approaches used to make this transformation, one is to approximate the relationship for a wavelength band by a function with the same form as the monochromatic Planck function. That is, the relationship between surface temperature and band integrated I_λ^B may be approximated as:

$$T_s = \frac{k_2}{\ln[k_1 / I_\lambda^B + 1]} \quad (5)$$

where T_s is surface temperature in Kelvin, I_λ^B is integrated band radiance from Eq. (2) (W m^{-2} sr^{-1} μm^{-1}), and k_1 and k_2 are "calibration" constants chosen to optimize the approximation for the band pass of the sensor. For Landsat 7, $k_1 = 666.09$ W m^{-2} sr^{-1} μm^{-1}, $k_2 = 1282.71$ K (http://ltpwww.gsfc.nasa.gov/IAS/handbook/handbook_toc.html); for Landsat 5, $k_1 = 607.76$ W m^{-2} sr^{-1} μm^{-1}, $k_2 = 1260.56$ K (Schneider & Mauser, 1996).

Thus, if band emissivity is known, the surface temperature can be calculated from Eqs. (1), (2), and (5). If it is assumed that the emissivity is 1.0 then $I_\lambda(0)$ is equal to $I_\lambda^B(T_s)$ and the surface temperature obtained from Eqs. (1), (2), and (5) is the same as the brightness temperature. However, when the emissivity is less than 1, the surface leaving radiance is reduced by the emissivity and increased by the reflected sky radiance. These must be estimated to approximate the actual surface temperature.

4.2. Calibration of Landsat 5 thermal data

O'Donnel (2001) found that temperature values derived from Landsat 5 thermal data have become cooler since it was launched in 1985. Hence, any calibration algorithms converting DN to radiance value require modification. His

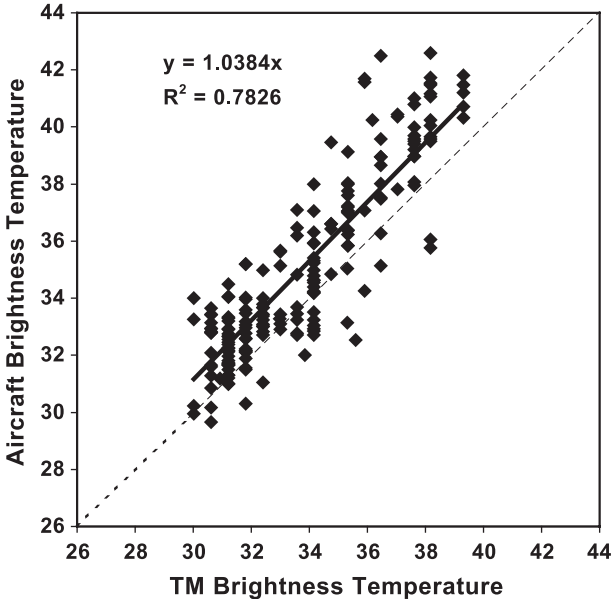

Fig. 3. Temperature comparison between aircraft measurement and Landsat 5 TM on June 23, 2002.

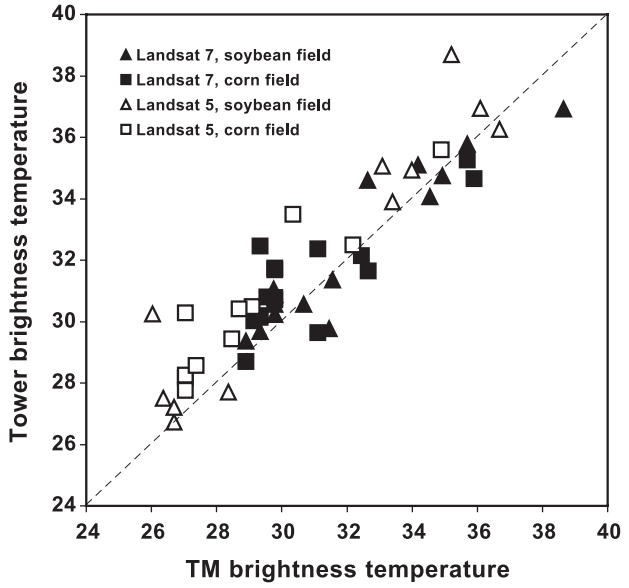

Fig. 4. Comparison of brightness temperature between Landsat TM/ETM and tower measurements.

results show that in 1999, Landsat 5 was underestimating by 1.18 °C compared with the Landsat 7 and ground measurements. Thus, the temperature data from Landsat 5 require additional calibration beyond the products provided.

For the thermal data, it is difficult to calibrate using other satellites or even ground observations because of the high spatial and temporal variations of surface temperature. Fortunately, during the SMEX02 experiment, synchronized low altitude aircraft measurements were available on June 23, 2002, which can be used for the calibration. Data from the aircraft and satellite are plotted in Fig. 3. Based upon the observed pattern, a linear regression with zero intercept function was fit to establish the following correction equation.

$$T_{B,AIR} = 1.0384 T_{B,TM} \quad (6)$$

where $T_{B,AIR}$ is aircraft brightness temperature, and $T_{B,TM}$ is TM brightness temperature. The resulting linear least squares regression yielded an $R^2 = 0.78$ and root-mean-square difference (RMSD) of approximately 1.5 °C.

Since the two sensors being compared have different bandpass widths (Landsat 10.4–12.5 μm and aircraft 9.6–11.5 μm), when the landcover emissivities are wavelength dependent, the sensors can have different effective emissivities and hence create a bias for the brightness temperature. Unfortunately, this error could not be excluded, which is discussed in the following section, although since the bandpasses are not too dissimilar and the emissivities are high it is not likely to have a major effect in our comparison.

Within the limitations discussed above, the results are consistent with those reported by O'Donnel (2001), implying that the satellite temperature is around 1.2 °C cooler when the observed surface brightness temperature is around 30 °C.

4.3. Brightness temperature extraction and comparison with tower measurements

From Eq. (5), the brightness temperature (T_B) for Landsat data at the surface was obtained through the atmospheric correction. In order to investigate the reliability of the atmospheric correction, TM/ETM brightness temperatures at the ground surface were compared with the tower measurements. At this point, only the accuracy of the atmospheric correction is considered. By using T_B measurements rather than T_s to compare the results, errors due to choice of emissivity and the sky radiance estimation were minimized—although the emissivity does affect our comparison, as we shall describe.

In Fig. 4, the Landsat T_B values are compared to the tower-based IRT measurements. This figure shows that most points are close to the 1:1 line, with RMSD = 1.5 °C and mean absolute difference (MAD) = 1.2 °C respectively for all the Landsat data, with RMSD = 1.2 °C and MAD = 1.0 °C for Landsat 7 and RMSD = 1.8 °C and MAD = 1.4 °C for Landsat 5. However, for some individual points, MAD reached 3–4 °C. These differences are due in part to the different wavelength bands. Radiometers on board the aircraft, the towers and on Landsat have different wavelength band passes, with 6–14 μm (filtered to 8–14 μm) for the tower based Apogee, 9.6–11.5 μm for the aircraft data and 10.4–12.5 μm for Landsat. If the land cover emissivity varies spectrally, this can lead to different T_B values being recorded for the same T_s. This difference is greatest for bare soil since soil emissivity can vary significantly over the wavelength range from 6 to 14 μm. In the SMEX02 watershed area, based on soil samples which were taken to be analyzed by the Jet Propulsion Labora-

Table 3
Atmospheric correction for Landsat 5 and 7 (visible bands)

Date	L_p (W m^{-2} sr^{-1} μm^{-1})		E_{dir} (W m^{-2} sr^{-1} μm^{-1})		E_{diff} (W m^{-2} sr^{-1} μm^{-1})		S		τ	
Channel	3	4	3	4	3	4	3	4	3	4
June 23, 2002	11.9275	3.8637	905.9411	659.8629	264.8494	120.6393	0.0992	0.0597	0.9052	0.9029
July 1, 2002	11.9486	3.9834	920.4499	678.6285	264.8016	123.5521	0.0991	0.0607	0.9052	0.9090
July 8, 2002	12.6030	4.3623	891.4602	650.6311	287.2881	139.0162	0.1044	0.0661	0.8986	0.8936
July 16, 2002	11.8540	3.8552	893.8681	651.2191	262.4292	119.6224	0.0988	0.0594	0.9056	0.9028
July 17, 2002	11.7550	3.9165	901.7579	660.9069	261.7690	121.6008	0.0981	0.0600	0.9052	0.9028

Table 4
Atmospheric correction, emissivity, and temperature of water for the ASTER thermal bands (July 1, 2002)

ASTER bands	I_λ (W m^{-2} sr^{-1} μm^{-1})	t_λ	d_λ (W m^{-2} sr^{-1} μm^{-1})	$I_{d\lambda}$ (W m^{-2} sr^{-1} μm^{-1})	ε_λ	λ (μm)	T_s (°C)
10	8.1588	0.493	3.5967	5.4795	0.9829	8.291	26.55
11	8.6879	0.613	2.8519	4.4435	0.9837	8.634	26.69
12	8.9734	0.688	2.3660	3.7861	0.9850	9.075	25.94
13	9.2663	0.672	2.7689	4.3504	0.9906	10.657	26.81
14	8.8790	0.627	3.0774	4.7266	0.9904	11.29	26.01

tory, soil emissivity is relatively high. Vegetation canopies have high effective emissivity at all wavelengths and soil emissivity is also high at most wavelengths (in the range 6–14 μm) being about 0.97 except for wavelengths between 8.1 and 9.7 μm, where the soil emissivity drops to 0.92–0.95 due to the presence of quartz. However, since the SMEX02 observations are over canopy covered surfaces, the emissivity error is relatively small and the greatest impact is most likely on the Apogee data. The comparison between T_B from Landsat and the tower measurements indicates similar results for both soybean and corn fields (Fig. 4). Hence, even though there is a fairly large difference in canopy cover between corn and soybean, which presumably would impact emissivity, there is no real effect on T_B.

There is a small effect on the measured T_B due to the differing instrument field of views. A wider angle might result in a T_B reduction. However, a significant source of discrepancies between tower and satellite T_B is likely due to the large differences in the pixel resolution of the sensors. As discussed in previous sections, tower-based IRT footprints are on the order of 1–3 m above the canopy, while Landsat TM has a 120-m, and ETM has a 60-m pixel resolution. Both Landsat resolutions are 1–2 orders of magnitude larger than the Apogee radiometer and sample a much larger area relative to the tower measurements. Hence, spatial variability in T_B at the meter resolution could contribute significantly to the scatter between Landsat and tower-based observations. Furthermore, errors associated with image georeferencing and in the atmospheric correction due to incomplete knowledge of the water vapor and aerosol profiles contribute to this scatter. However, given all of these sources of uncertainty, the differences illustrated in Fig. 4 are similar to those found in other studies (Gillespie et al., 1998).

5. Surface emissivity estimation

5.1. Background and methods

Emissivity information is required to convert brightness temperature to kinetic surface temperature. As mentioned previously, there are several methods to retrieve surface emissivity. However, these methods are only suitable for multi-band satellites, such as ASTER or MODIS. Since Landsat has only a single window for thermal data, it is impossible to obtain emissivity directly for TM/ETM data without using other spectral bands and/or ancillary data and assumptions.

One technique for estimating emissivity that can be applied is a fractional cover mixture model. It is assumed that the soil background and the vegetation have specific known emissivities and that they "mix" according to the fractional cover (Sobrino et al., 2001). The fractional vegetation cover is then estimated from the NDVI. Some investigators have also established empirical models between NDVI and emissivity (Valor & Caselles, 1996; Van de Griend & Owe, 1993).

If the surface is homogeneous and flat, then the basic equation can be expressed as (Sobrino et al., 2001):

$$\varepsilon_\lambda \approx \varepsilon_v f_v + (1 - f_v)\varepsilon_s \quad (7)$$

where ε_λ is the composite emissivity, ε_v is the vegetation emissivity, ε_s is the soil emissivity, and f_v is the fractional vegetation cover.

Here, the soil emissivity was based upon laboratory analysis of soil samples collected in the watershed. The average value for the Landsat thermal band is 0.978. The vegetation emissivity (ε_v) may be estimated as 0.985 (Sobrino et al., 2001).

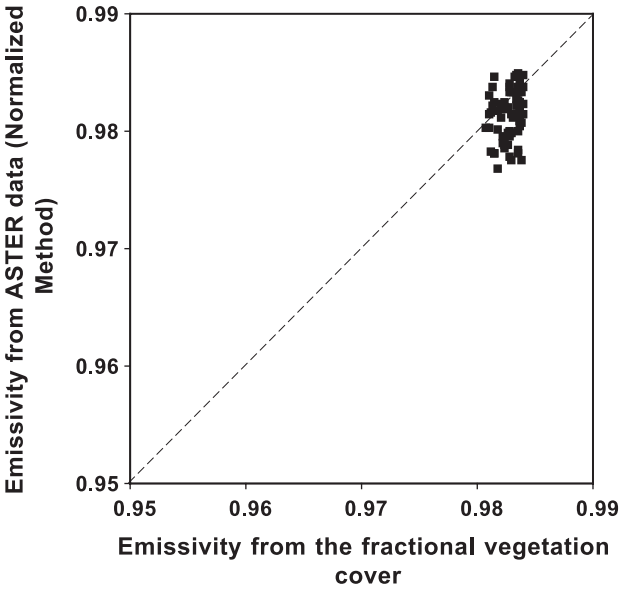

Fig. 5. Emissivity estimation based upon two different methods.

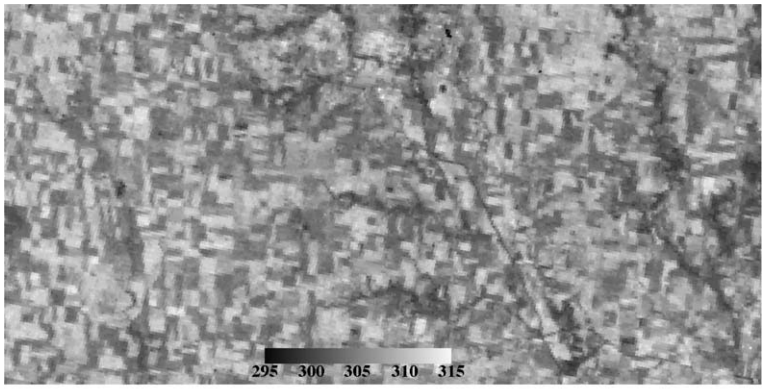

June 23, 2002

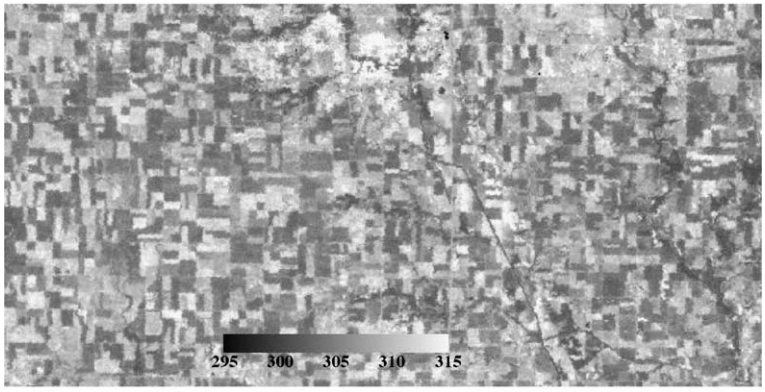

July 1, 2002

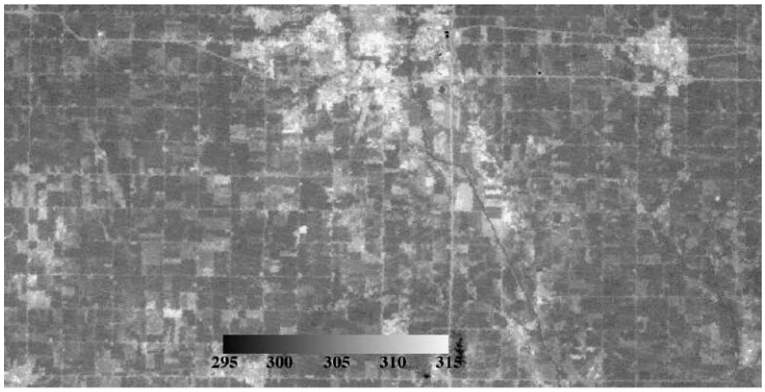

July 8, 2002

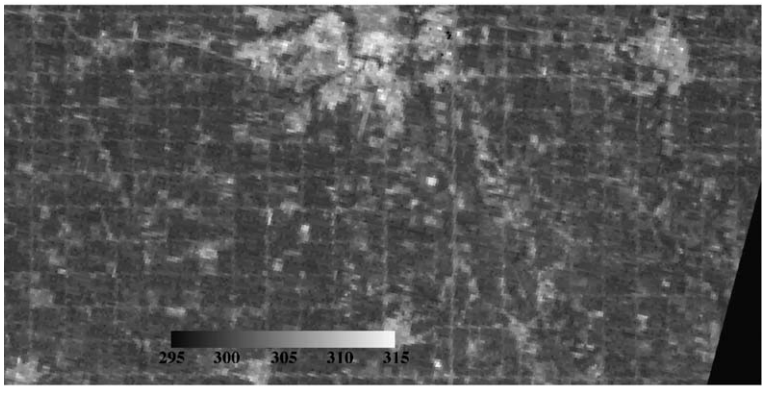

July 16, 2002

Fig. 6. Land surface temperature images derived from TM/ETM images over the watershed area.

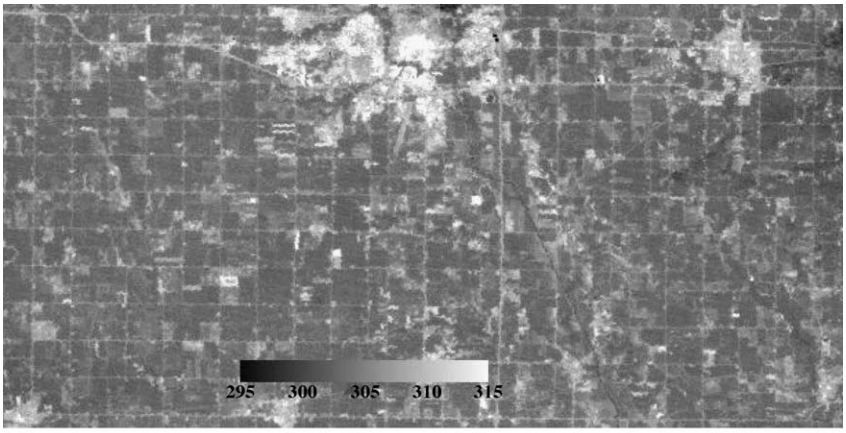

Fig. 6 (*continued*).

5.2. NDVI data source

Landsat visible and near-infrared bands were used to compute the Normalized Difference Vegetation Index (NDVI) as follows:

$$\mathrm{NDVI} = \frac{\rho(\mathrm{band4}) - \rho(\mathrm{band3})}{\rho(\mathrm{band4}) + \rho(\mathrm{band3})} \tag{8}$$

where ρ is band reflectance.

These bands must also be atmospherically corrected before applying Eq. (8). For these bands, the atmospheric correction is affected more by aerosols than the thermal bands.

If the area surrounding a target is assumed to be the same as (or similar to) the target and the target is assumed to be Lambertian and uniform, the reflectance at the target can be expressed conveniently as (Adler-Golden et al., 1999; Vermote & Vermeulen, 1999; Vermote et al., 1997):

$$\rho = \frac{\pi(L_t - L_p)}{(E_{dir} + E_{diff})\tau + \pi S(L_t - L_p)} \tag{9}$$

where ρ is reflectance, L_t is the satellite-based radiance, S is the reflectance of the atmosphere, L_p is the atmospheric path radiance, E_{dir} is the direct irradiance at the surface, E_{diff} is the diffuse irradiance at the surface, and τ is the total diffuse transmittance from the ground to the top of the atmosphere in the view direction of the satellite.

Using the same atmospheric correction model information in MODTRAN as for the thermal bands with a default aerosol profile from the model, we can obtain S, L_p, E_{dir}, E_{diff}, and τ. These are listed in Table 3.

Even when the assumptions described above are not fully applicable or the atmospheric conditions are not precisely known, the formula provides a useful normalization of the data and was used here to standardize the NDVI index. Additional details on the processing of these bands are provided in Jackson et al. (2004).

Choudhury et al. (1994) found that the relationship between NDVI and fractional cover can often be expressed as:

$$f_v = 1 - \left(\frac{\mathrm{NDVI}_{max} - \mathrm{NDVI}}{\mathrm{NDVI}_{max} - \mathrm{NDVI}_{min}}\right)^a \tag{10}$$

where NDVI_{max} is the NDVI for complete vegetation cover and NDVI_{min} is NDVI for bare soil. In this paper, NDVI_{max} and NDVI_{min} were assigned values of 0.94 and 0.0, respectively, based upon NDVI values derived from several days of TM/ETM data. The coefficient a is a function of leaf orientation distribution within the canopy, where erectophile to planophile canopies have values between 0.6 and 1.25. A value of 0.6 was used in the current investigation. The fractional vegetation cover was compared with limited ground observations and the results were consistent. Emissivity was then estimated using the derived fractional vegetation cover and the specified emissivity values of soil and vegetation.

5.3. Emissivity from ASTER

Emissivity estimated based upon fractional vegetation cover could not be directly evaluated with ground-based observations. However, we were able to compare these estimates with those derived using multichannel band thermal-IR data. It should be noted that it is difficult if not impossible to judge which method is more reliable without more information or a data set where there is greater variation in emissivity.

The multichannel thermal data used were collected by ASTER on July 1, 2002 very close in time to the Landsat 7 overpass, thus providing the satellite data needed to compare the two techniques for estimating emissivity. The ASTER data were version 2.06. Here, the normalized method was used to extract emissivity from the ASTER

data. Details on how to use the method can be found in Gillespie (1985) and Realmuto (1990). The maximum emissivity is assumed as 0.985, which is the vegetation emissivity in Eq. (7).

Before using this method, we checked both the atmospheric correction and the calibration of the ASTER image by taking 3×3 arrays of pixels from the central area of a lake and averaging the radiance so that noise from the image is reduced and the radiance truly represents the water radiance. The method used for atmospheric correction of the ASTER data was the same as that used for the TM/ETM data. Following atmospheric correction, the brightness temperatures of channels 10 and 11 were compared. Emissivities of the two channels were expected to be similar so only variation in water vapor should create a difference. We found that the water vapor originally used should have been slightly lower. Therefore, the adjusted water vapor profile was used for both ETM and ASTER data. Following this, the emissivity of water for the ASTER bands was obtained from http://speclib.jpl.nasa.gov. Using the adjusted atmospheric water vapor amount, the water temperature was obtained from the five channels using Eqs. (1), (2), and (5), where k_1 and k_2 were calculated from ASTER central wavelengths (Table 4). The results of this algorithm are listed in Table 4.

Theoretically, the water temperature should be the same for the five channels. Table 4 shows that the temperatures from channels 12 and 14 were over 0.5 °C cooler compared with other channels. These differences could not be explained by incorrect atmospheric corrections. This indicates that the ASTER data for these two channels required an additional calibration. Assuming that the average temperature from the five channels could be regarded as the true water temperature, the calibration coefficients for the five channels can be adjusted to achieve the balance. These calibration coefficients were then applied to the whole image.

5.4. Emissivity comparison between ASTER and NDVI

The emissivity comparison between the values derived from fractional vegetation cover and those from the ASTER normalized method over the watershed area is shown as Fig. 5. In the figure, the emissivity from ASTER is the average of channels 13 and 14 which, when combined, have a similar wavelength bandwidth to the TM/ETM thermal band. Points in the figure were selected from the 31 watershed sites. Since the ASTER narrow bands had some noise (stripes in the image), the sites located on the stripes were excluded. Fig. 5 shows that the results from the two different methods were close and that the emissivity from the normalized method has a larger spatial variation. The similarity in results gives us confidence in using the simpler and more extendable fractional vegetation cover method of estimating emissivity in this investigation.

6. Surface temperature products

Combining the emissivity estimates with Eqs. (1), (2), and (5), T_s can be computed. The five TM/ETM T_s images are displayed in Fig. 6. For June 23 and July 1, the images show that the T_s and its spatial variation were high. On these two days, the weather was clear, and the soil dry, especially on July 1. But for July 8, July 16, and July 17, both T_s and its spatial variation were lower. For July 8 and July 17, a small fraction of the image had cloud cover.

The spatial and temporal variations in T_s reflect the different cover types, the changing fractional vegetation cover f_v, and the available soil moisture. For the June 23, f_v for corn and soybean was nominally 0.4–0.6. T_s values for this image were relatively high as the result of high soil temperatures. Due to dry surface moisture condition the spatial variation of T_s was a function of crop type. The corn fields had higher f_v, especially after July 1 when f_v was around 0.8. With adequate moisture in the root zone and high f_v, this produced lower T_s values. Also notice that T_s in urban areas and at road intersections were significantly higher than the surrounding crop areas (Fig. 6 and Table 5), especially after July 8. This is primarily due to the soybean and corn crops reaching near full cover ($f_v \sim 1$), whereas the roads and urban areas still contain a significant fraction of bare soil, and/or non-transpiring surface (i.e., roof tops, concrete, and asphalt). The results from Table 5 were calculated using the classified image. Most of the pixels classified as corn and soybean contain that single land cover type. However, most road surfaces and urban area pixels contain a mixture of vegetation, bare soil, and manmade surfaces (e.g., concrete). Therefore, actual T_s for purely road surfaces and building roof tops are likely to be higher than indicated by the pixel integrated value.

The spatial and temporal variations in T_s also reflect surface soil moisture variations. On days with lower soil

Table 5
Spatial statistics of 5 days of land surface temperature data

Date	Maximum (K)	Minimum (K)	Average (K)	Standard deviation (K)	Average corn (K)	Average soybean (K)	Average road and urban (K)
June 23	315.73	289.00	306.53	2.79	305.40	308.85	306.71
July 1	322.76	283.54	307.73	3.13	305.88	309.87	308.92
July 8	328.47	290.11	305.10	2.41	303.97	305.20	307.37
July 16	317.70	289.14	301.40	2.22	300.49	301.26	303.77
July 17	329.63	290.83	304.76	2.58	303.53	304.76	307.64

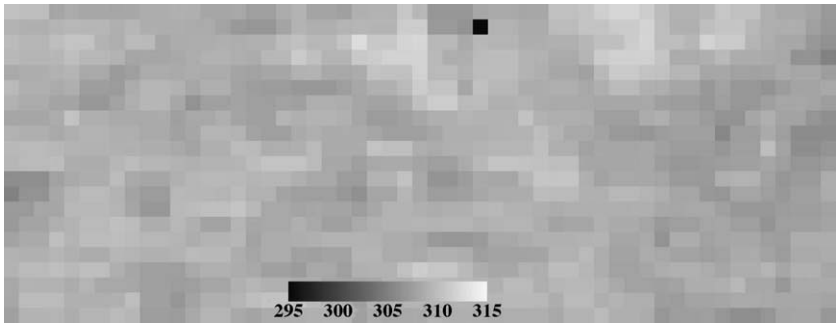

Fig. 7. MODIS derived land surface temperature of the watershed area on July 1, 2002.

moisture levels, such as on July 1, 2002, T_s values were higher in contrast to days following precipitation events, such as July 8. In addition, the higher surface moisture significantly reduced spatial variation and contrast in T_s (Table 5). Since TM has a 120-m resolution (June 23 and July 16, 2002), the data range and spatial variations were smaller than these observed for the 60-m resolution ETM data. The T_s values in Table 5 are comparable only for images having the same pixel resolution, namely July 1, July 8, and July 17 from ETM, and June 23 and July 16 from TM.

7. Scale analysis

For the lower pixel resolution imagery from MODIS and AVHRR, although they are more useful for operational monitoring purposes, detailed spatial variations of T_s within and between individual fields will not be detectable because typical field sizes for many agricultural regions have dimensions on the order of 10^2 m, whereas MODIS and AVHRR thermal data have a pixel resolution on the order of 10^3 m. The MODIS T_s image of the watershed area on July 1, 2002 (Fig. 7) illustrates how much of the detailed spatial distribution of T_s is no longer present when compared to Landsat 7 (Fig. 6). The image is a MODIS T_s product (http://www.icess.ucsb.edu/modis/LstUsrGuide/usrguide.html) made available to the project by M. Friedl, Boston University. Compared with the Landsat 7 ETM temperature image shown in Fig. 6, there is much less spatial structure, with no discrimination of field boundaries due to the low resolution. Thomas et al. (2002) observed a similar result when they analyzed coastal sea surface temperature variability using Landsat and AVHRR data.

Direct quantitative comparison between MODIS and TM/ETM T_s values is not possible because MODIS data are acquired ~ 30 min after the Landsat overpass. During summer, T_s changes rapidly in the mid morning period of 10:40 to 11 AM local standard time. Ground-based observations indicated the brightness temperature difference between the Landsat overpass and the Terra overpass times can range from 0.8 to 2.0 °C, depending on the vegetation cover. Instead, we resampled or averaged the TM/ETM T_s data to represent MODIS pixel resolution observations. An analysis of the resolution effects on T_s was conducted using the Landsat data. A 304×304 block of pixels (60-m resolution) was extracted from the July 1, 2002 Landsat 7 T_s and NDVI images over the watershed area and converted to a coarser resolution of 960 m (19×19 pixels), which is similar to the MODIS thermal-infrared resolution. Table 6 lists the statistical results obtained using the two different scales of images.

The results shown in Table 6 indicate that when the resolution changes from 60 to 960 m, both the spatial standard deviation (σ) and range in T_s are dramatically reduced. The σ for the 960-m resolution image is nearly half that of the 60-m resolution image for both NDVI and T_s. This means that at such coarse resolutions, such as MODIS T_s data, much of the spatial pattern in T_s due to variations in land cover type and condition is lost. This loss of critical information with resolution has been discussed by Townshend and Justice (1988) who argued that spatial resolutions of 250–500 m are needed to monitor land-use and land-cover changes brought about by human activities. Moreover, when sub-pixel variability in T_s and f_v is significant, this can lead to significant errors in pixel-average surface energy balance estimation (Kustas & Norman, 2000).

To confirm that the conclusions in regard to MODIS are reasonable, we compared the scaling of MODIS and ASTER T_s. As described above, a small area of the WC was used for the analysis. ASTER data had a 90-m resolution which is between the resolutions of the Landsat ETM and TM. However, unlike Landsat, the ASTER data were obtained as the same time as the MODIS. Unfortunately, only one ASTER image collected on July 1, 2002 was

Table 6
Statistical comparison of Landsat derived products at different spatial resolutions on July 1, 2002

	Resolution (m)	Maximum	Minimum	Average	Standard deviation
Temperature (K)	60	322.76	299.30	307.90	3.09
	960	312.73	304.38	307.90	1.56
NDVI	60	0.9314	0.0929	0.7324	0.1338
	960	0.8622	0.3562	0.7324	0.0760

available. The ASTER T_s were resampled to a 926-m resolution, which is the resolution of the MODIS T_s product we have. In order to make the two data sets spatially comparable, the MODIS data were reprojected to the UTM system. The mean and the σ for the two data sets are listed in Table 7. The research area in this comparison was slightly different from the one that was used for Table 6 because the ASTER image did not fully cover the watershed area. The results in Table 7 indicate that σ at the high resolution of ASTER T_s is more than twice that of the lower-resolution MODIS T_s observations. These results are consistent with the scaling analysis performed with the Landsat data.

In Table 7, there is $\sim$ 0.5 K difference in average T_s for the two data sets. A pixel by pixel T_s comparison between the MODIS and ASTER is illustrated in Fig. 8. RMSD and MAD are 0.9 and 0.7 K, respectively. Some pixels reach a $\sim$2 K difference for the two data sets. This is largely due to the different sensors, georeferencing, and differences in atmospheric and emissivity corrections algorithms used to derive T_s. The MODIS T_s data were obtained from a system generating an operational product, while ASTER T_s data were processed using local atmospheric observations with the procedure outlined in previous sections.

The spatial and temporal variation observed in Landsat and ASTER data is useful for interpreting within-pixel variations from MODIS resolutions. For estimating fluxes, the impact of using MODIS versus Landsat resolution T_s data is investigated by Kustas et al. (2004). A key result from this study is that using 10^3-m resolution T_s data, one cannot distinguish a variation in fluxes, particularly evapotranspiration between soybean and corn fields. A possible procedure for recovering fluxes of individual fields is to make use of a procedure described by Kustas et al. (2003) for sharpening the resolution of thermal band data to that of visible/near-infrared bands, using the functional relationship between surface temperature and vegetation indices. The Landsat and ASTER data can be used to evaluate such sharpening procedures, and the resulting accuracy in surface flux estimation at the higher resolutions.

8. Error analysis

The conversion of the radiances to land surface temperature involves a number of assumptions and approximations. There are three sources of error, one comes from sensor properties (calibration, assumption from broad band to single band), a second from atmospheric correction (radiative transfer model MODTRAN 4.1 and water vapor), and the third from estimating surface emissivity.

Table 7
Statistical comparison of ASTER temperature and MODIS derived temperature on July 1, 2002

Sensors	Resolution (m)	Maximum (K)	Minimum (K)	Average (K)	Standard deviation (K)
ASTER	90	324.24	292.91	309.35	3.50
	926	313.94	302.21	309.30	1.49
MODIS	926	312.62	302.50	308.83	1.15

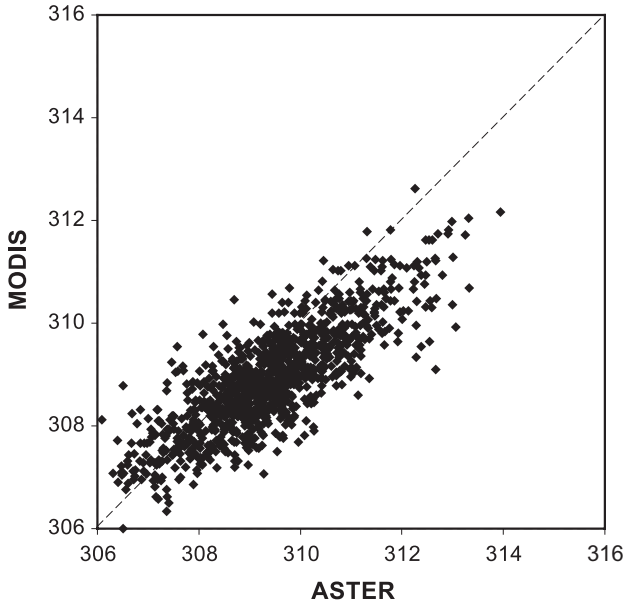

Fig. 8. Land surface temperature comparison between MODIS and ASTER at a 926-m resolution on July 1, 2002.

The error from using Eq. (5) is difficult to quantify, but should be relatively minor. As for the calibration error, Barsi et al. (2003) showed that the error is within $\pm$0.6 K for ETM obtained after December 2000. For Landsat 5 TM data, calibration error is more difficult to quantify but other studies indicated it is significant and requires recalibration with on site data (O'Donnel, 2001), as performed here with the aircraft observations.

Assuming that the error from the MODTRAN algorithms is small, provided the input information is accurate, atmospheric correction error arises mainly from the accuracy of water vapor measurements. We have made an assumption that it is nominally 10% (Schmugge et al., 1998). If the target temperature is 300 K brightness temperature, this could lead to a brightness temperature error of around 0.5 K.

The emissivity error can come from the NDVI estimation error and the use of the approximate Eqs. (7), (9), and (10). T_s values are sensitive to the emissivity (Van de Griend & Owe, 1993). Fortunately, the emissivity of the soil is relatively high at this site and is also vegetated which

Table 8
Error analysis for ETM land surface temperature estimation

Sensor calibration error	Eq. (5) and sensor calibration	0.6 (K)
Atmospheric correction error	MODTRAN 4.1 and water vapor	0.5 (K)
Emissivity error	NDVI, Eqs. (7), (9), and (10)	0.2 (K)

resulted in the general applicability of an emissivity of about ~ 0.98. The emissivity error for this site should be less than 0.005 which could lead to a change of 0.2 K in the land surface temperature when the target brightness temperature is 300 K. The result of using these assumptions and the error levels associated with them are summarized in Table 8 for Landsat ETM data. The total error is similar to the approximately 1 K difference obtained in comparisons with the tower and satellite data.

9. Discussions and conclusions

The findings from this investigation show that it is possible to extract accurate land surface temperature of about 1 K from Landsat TM/ETM data with a radiative transfer model (MODTRAN 4.1), on site radiosonde data, and an emissivity algorithm. The brightness temperatures derived from Landsat satellite measurements were compared with ground measurements. The results of the comparison suggest that the average difference is 0.98 °C for Landsat 7 and 1.47 °C for Landsat 5. Considering the potential bias in the actual atmospheric profile information, the different wavelength bands and footprint sizes, the results are reasonable and consistent with the accuracy found in other studies (Gillespie et al., 1998).

Emissivity was determined using the fractional area average of canopy emissivity and soil emissivity. f_v was estimated by satellite-derived NDVI. In the SMEX02/SMACEX field experiment, this method is a reasonable approximation due to the high soil emissivity. The emissivity derived from f_v was compared with values derived from an ASTER image using the normalized method. The results show that the difference is within 0.01, although the overall variation is too small to draw any general conclusions. Based on this result, f_v was used to estimate the emissivity over the entire SMEX02/SMACEX study area.

From these results, we conclude that with adequate ancillary information and atmospheric correction, the high-resolution TM/ETM data can be used to extract detailed information about vegetation cover and surface temperature. These are both important surface boundary conditions for modeling surface fluxes. At the higher spatial resolution of Landsat, this information can be used to assess crop conditions within fields and the impacts of land cover and land use changes on surface energy balance. In addition, because MODIS images are acquired about 30 min after ETM, the Landsat data provide excellent validation of the broader scale data as well as information about the effects of subpixel variability on surface flux estimation (Kustas & Norman, 2000).

The five images of T_s from the SMEX02/SMACEX field experiment covered a period from June 23, 2002 to July 17, 2002. These high-resolution T_s images show that T_s changed with f_v and surface soil moisture conditions. With the higher f_v and/or high surface moisture (particularly for the images after July 1) the magnitude and spatial variability in T_s were relatively low. The spatial variation in T_s also responded to the different types of land cover. It has been shown that many of the details of spatial and temporal variation cannot be accessed at the lower spatial resolution thermal infrared images, such as MODIS and AVHRR.

Routine T_s data must rely on lower-resolution satellite data, such as AVHRR, MODIS, and GOES. These data can provide daily to half-hourly coverage. They are appropriate for operational monitoring, but the low spatial resolution limits their use for detailed spatial analysis of land cover changes and states in intensively managed and fragmented agricultural areas such as Iowa (Kustas et al., 2003). When subpixel variability in f_v and T_s is significant, large errors in pixel average flux estimation can result. Landsat and ASTER data offer higher spatial resolution data, but are available on a biweekly basis at best. Recently, there has been an effort to merge the high temporal/low spatial resolution with high spatial/low temporal resolution satellite data in a nested-scale flux modeling system (Norman et al., 2003). This modeling framework used in concert with the thermal sharpening scheme of Kustas et al. (2003) may be one of the more effective modeling systems for providing both routine and high spatial resolution data necessary for monitoring agricultural conditions at the field scale. Landsat TM and ETM data and coincident MODIS and ASTER data provide a framework to evaluate these techniques.

Acknowledgements

This research was supported by the NASA EOS Aqua AMSR, Terrestrial Hydrology, Global Water and Energy Cycle Programs. We thank all the cooperators and participants in SMEX02. The helpful comments and advice from the three anonymous reviewers are very gratefully acknowledged.

References

Adler-Golden, S. M., Matthew, M. W., Bernstein, L. S., Levine, R. Y., Berk, A., Richtsmeier, S. C., Acharya, P. K., Anderson, G. P., Felde, G., Gardner, J., Hoke, M., Jeong, L. S., Pukall, B., Mello, J., Ratkowski, A., & Burke, H.-H. (1999). Atmospheric correction for short-wave spectral imagery based on MODTRAN4. *SPIE Proceeding, Imaging Spectrometry V, 3753*, 61–91.

Barsi, J. A., Schott, J. R., Palluconi, F. D., Helder, D. L., Hook, S. J., Markham, B. L., & Chander, G. (2003). Landsat TM and ETM+ thermal band calibration. *Canadian Journal of Remote Sensing*, *29*, 141–153.

Becker, F., & Li, Z. (1990). Towards a local split window method over land surfaces. *International Journal of Remote Sensing*, *11*, 369–393.

Berk, A., Bernstein, L. S., Anderson, G. P., Acharya, P. K., Robertson, D. C., Chetwynd, J. H., & Adler-Golden, S. M. (1998). MODTRAN cloud and multiple scattering upgrades with application to AVIRIS. *Remote Sensing of Environment*, *65*, 367–375.

Bresnahan, P. A., & Miller, D. R. (1997). Choice of data scale: Predicting resolution error in a regional evapotranspiration model. *Agricultural and Forest Meteorology*, *84*, 97–113.

Bugbee, B., Droter, M., Monje, O., & Tanner, B. (1999). Evaluation and modification of commercial infrared-red transducers for leaf temperature measurement. *Advances in Space Research*, *22*, 1425–1434.

Choudhury, B. J., Ahmed, N. U., Idso, S. B., Reginato, R. J., & Daughtry, C. S. T. (1994). Relations between evaporation coefficients and vegetation indices studied by model simulation. *Remote Sensing of Environment*, *50*, 1–17.

Gillespie, A. R. (1985). Lithologic mapping of silicate rocks using TIMS. In: *TIMS data users' workshop. JPL Publication, vol. 86-38* (pp. 29–44). Pasadena, CA: Jet Propulsion Laboratory.

Gillespie, A., Rokugawa, S., Matsunaga, T., Cothern, J. S., Hook, S., & Kahle, A. B. (1998). A temperature and emissivity separation algorithm for Advanced Spaceborne Thermal Emission and Reflection Radiometer (ASTER) images. *IEEE Transactions on Geoscience and Remote Sensing*, *36*, 1113–1126.

Jackson, T. J., Chen, D., Cosh, M. H., Li, F., Walthall, C., Anderson, M., & Doraiswamy, P. (2004). Vegetation water content mapping using Landsat TM derived NDWI for corn and soybean. *Remote Sensing of Environment*, *92*, 476–473 (doi:10.1016/j.rse.rse.2003.10.021).

Kahle, A. B., Madura, D. P., & Soha, J. M. (1980). Middle infrared multispectral aircraft scanner data: Analysis for geological application. *Applied Optics*, *19*, 2279–2290.

Kealy, P. S., & Gabell, A. R. (1990). Estimation of emissivity and temperature using alpha coefficients. In: *Proc. 2nd TIMS workshop. JPL Publication, vol. 90-55* (pp. 11–15). Pasadena, CA: Jet Propulsion Laboratory.

Kustas, W. P., Li, F., Jackson, T. J., Prueger, J. H., MacPherson, J. I., & Wolde, M. (2003). Effect of remote sensing pixel resolution on energy balance modeling of croplands in Iowa. *Remote Sensing of Environment*, *92*, 536–548 (doi:10.1016/j.rse.2004.10.020).

Kustas, W. P., & Norman, J. M. (1996). Use of remote sensing for evapotranspiration monitoring over land surfaces. *Hydrological Sciences Journal*, *41*, 495–516.

Kustas, W. P., & Norman, J. M. (2000). Evaluating the effects of subpixel heterogeneity on pixel average fluxes. *Remote Sensing of Environment*, *74*, 327–342.

Kustas, W. P., Norman, J. M., Anderson, M. C., & French, A. N. (2003). Estimating subpixel surface temperatures and energy fluxes from the vegetation index-radiometric temperature relationship. *Remote Sensing of Environment*, *85*, 429–440.

Li, Z., Becker, F., Stoll, M. P., & Wan, Z. (1999). Evaluation of six methods for extracting relative emissivity spectra from thermal infrared images. *Remote Sensing of Environment*, *69*, 197–214.

MacPherson, J.L., & Wolde, M. (2002). NRC Twin Otter operations in the Soil Moisture–Atmosphere Coupling Experiment (SMACEX). National Council Canada(26 pp.). Report LTR-FR-190, Institute for Aerospace Research, Ottawa, Ontario, Canada.

Norman, J. M., Anderson, M. C., Kustas, W. P., French, A. N., Mecikalski, J., Torn, R., Diak, G. R., Schmugge, T. J., Tanner, B. C. W. (2003). Remote-sensing of surface energy fluxes at 10^1-m pixel resolutions. *Water Resource Research*, *39*(8), 1221 (doi:10.1029/2002WR001775.2003).

O'Donnel, E. (2001). Thermal calibration of Landsat 5 using Great Lakes imagery, http://www.cis.rit.edu/~emo1683/senres/ppframe.htm

Price, J. C. (1983). Estimating surface temperature from satellite thermal infrared data—a simple formulation for the atmospheric effect. *Remote Sensing of Environment*, *13*, 353–361.

Qin, Z., Karnieli, A., & Berliner, P. (2001). A mono-window algorithm for retrieving land surface temperature from Landsat TM data and its application to the Israel–Egypt border region. *International Journal of Remote Sensing*, *18*, 3719–3746.

Realmuto, V. J. (1990). Separating the effects of temperature and emissivity: Emissivity spectrum normalization. In: *Proc. 2nd TIMS workshop. JPL Publication, vol. 90-55* (pp. 31–37). Pasadena, CA: Jet Propulsion Laboratory.

Schmugge, T., French, A., Ritchie, J. C., Rango, A., & Pelgrum, H. (2002). Temperature and emissivity separation from multispectral thermal infrared observations. *Remote Sensing of Environment*, *79*, 189–198.

Schmugge, T., Hook, S. J., & Coll, C. (1998). Recovering surface temperature and emissivity from thermal infrared multispectral data. *Remote Sensing of Environment*, *65*, 121–131.

Schneider, K., & Mauser, W. (1996). Processing and accuracy of Landsat Thematic Mapper data for lake surface temperature measurement. *International Journal of Remote Sensing*, *17*, 2027–2041.

Sobrino, J. A., Raissouni, N., & Li, Z. (2001). A comparative study of land surface emissivity retrival from NOAA data. *Remote Sensing of Environment*, *75*, 256–266.

Thomas, A., Byrne, D., & Weatherbee, R. (2002). Costal sea surface temperature variability from Landsat infrared data. *Remote Sensing of Environment*, *81*, 262–272.

Townshend, J. G. R., & Justice, C. O. (1988). Selecting the spatial resolution of satellite sensors required for global monitoring of land transformations. *International Journal of Remote Sensing*, *9*, 187–236.

Valor, E., & Caselles, V. (1996). Mapping land surface emissivity from NDVI: Application to European, African, and South American areas. *Remote Sensing of Environment*, *57*, 167–184.

Van de Griend, A. A., & Owe, M. (1993). On the relationship between thermal emissivity and the Normalized Difference Vegetation Index for natural surfaces. *International Journal of Remote Sensing*, *14*, 1119–1131.

Vermote, E. F., Saleous, N. E., Justice, C. O., Kaufman, Y. J., Privette, J. L., Remer, L., Roger, J. C., & Tanre, D. (1997). Atmospheric correction of visible to middle-infrared EOS-MODIS data over land surfaces: Background, operational algorithm and validation. *Journal of Geophysical Research*, *102*, 17131–17141.

Vermote, E. F., & Vermeulen, A. (1999). Atmospheric correction algorithm: Spectral reflectances (MOD09), Algorithm Technical Background. Available at: http://modarch.gsfc.nasa.gov/MODIS/ATBD/atbd_mod08.pdf

Wan, Z., Zhang, Y., Zhang, Q., & Li, Z. (2002). Validation of the land-surface temperature products retrieved from Terra Moderate Resolution Imaging Spectroradiometer data. *Remote Sensing of Environment*, *83*, 163–180.

Watson, K. (1992). Spectral ratio method for measuring emissivity. *Remote Sensing of Environment*, *42*, 113–116.